Electronic Supplementary Material (ESI) for Journal of Materials Chemistry A.

A Robust and Highly Active Hydrogen Evolution Catalyst Based on Ru Nanocrystals supported on Vertically Oriented Cu Nanoplates

Dipak V. Shinde[a]*, Tathiana Midori Kokumai[b], Joka Buha[a] Mirko Prato[c], Luca De Trizio[a]*, Liberato Manna[a]*

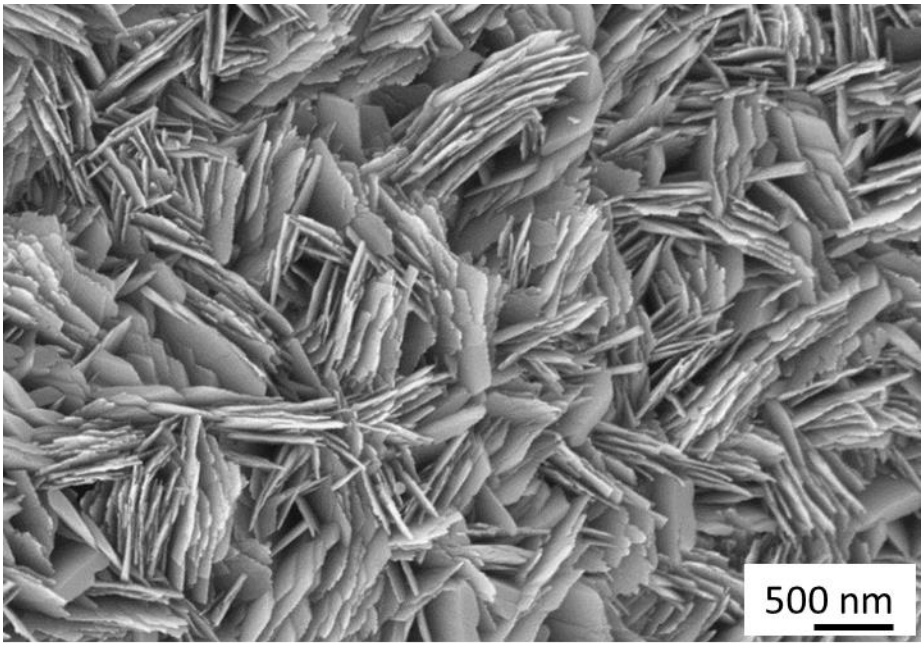

Figure S1. SEM image of CuO NPs deposited on Ti substrate.

X-ray Diffraction (XRD). The as prepared Cu-Ru/Ti electrode was directly used for XRD measurements. The electrode was placed on a zero-diffraction silicon wafer for measurements. A PANalytical Empyrean X-ray diffractometer with a 1.8 kW Cu Kα ceramic X-ray tube and PIXcel3D 2 × 2 area detector operating at 45 kV and 40 mA was used to collect diffraction patterns. The samples were put on zero diffraction single-crystal quartz substrates. The diffraction patterns were collected at room temperature in air using a parallel-beam (PB) geometry and a symmetric reflection mode. The data analysis was performed with the HighScore 4.1 software obtained from PANalytical.

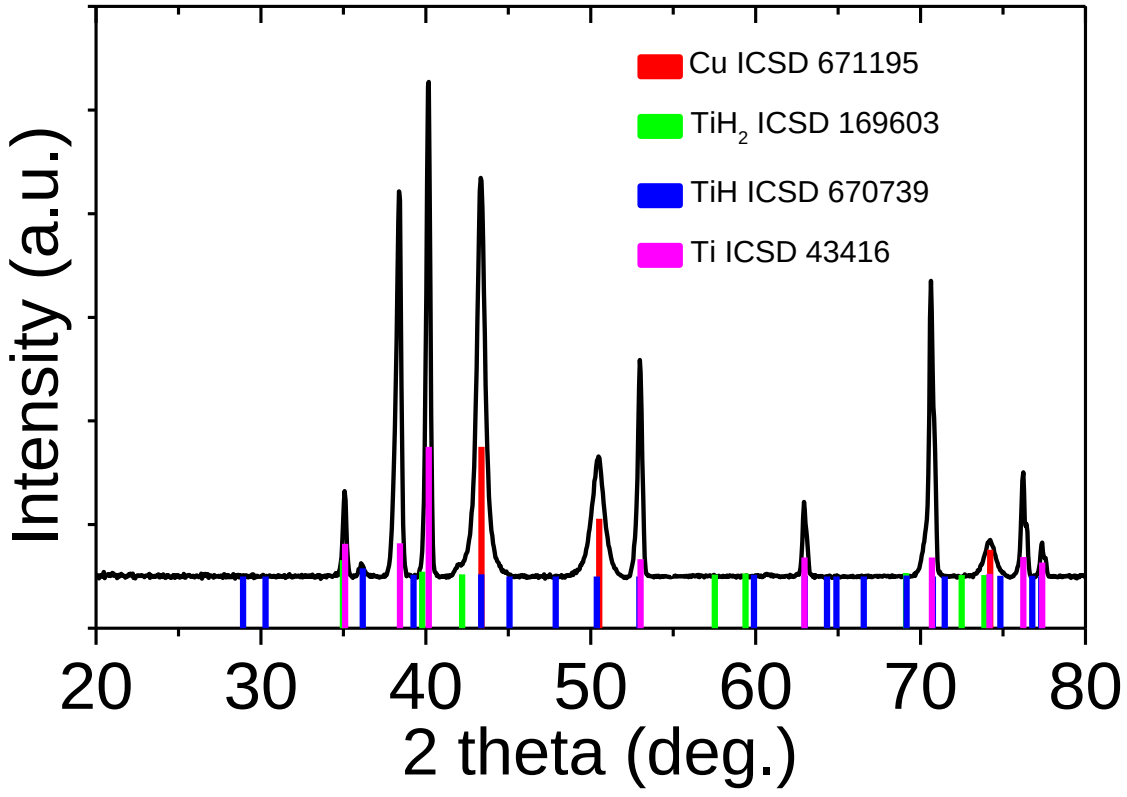

Figure S2. XRD analysis of the as prepared Cu-Ru/Ti electrode. The corresponding bulk reflections of Cu, Ti, TiH_2 and TiH phases are shown for comparison.

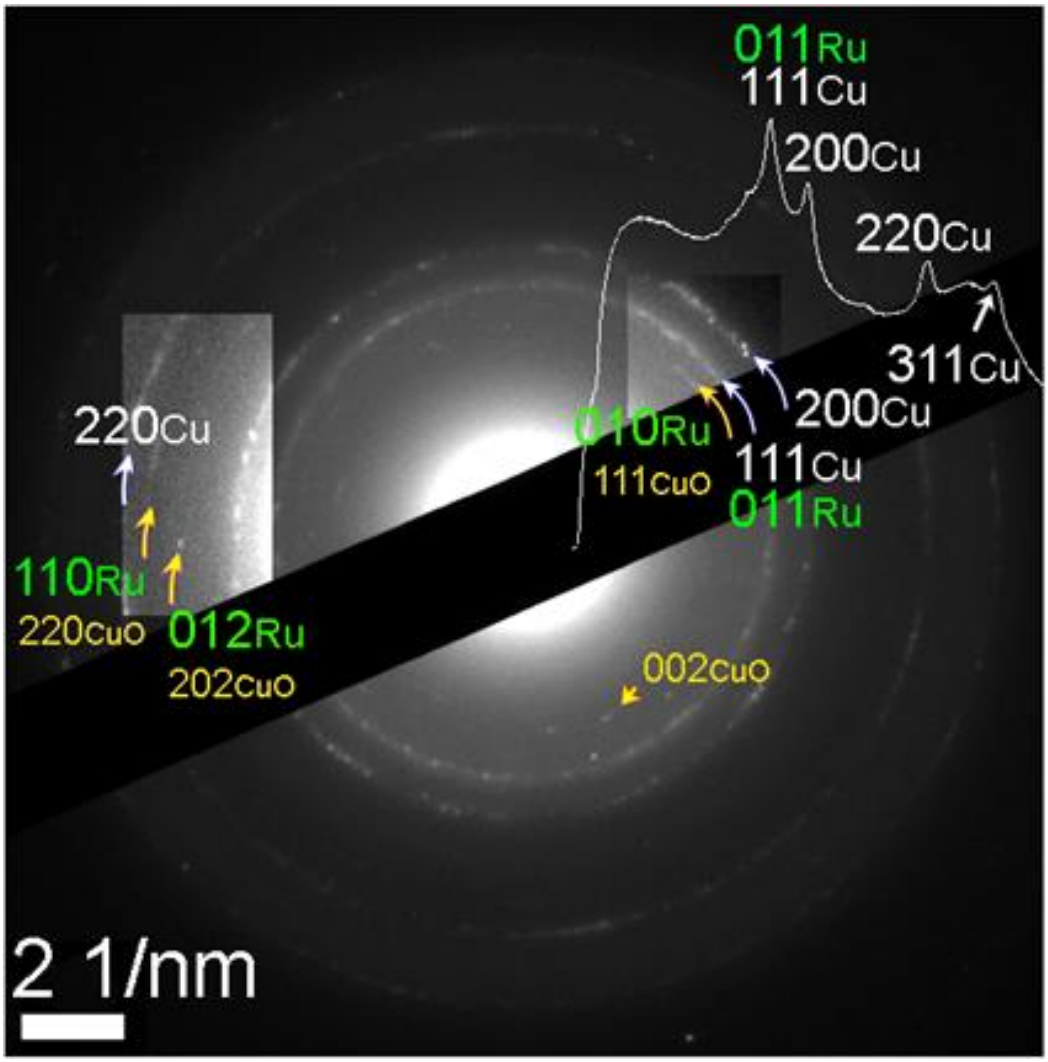

Figure S3. Selected area TEM electron diffraction pattern recorded from a fragment of the catalyst. The intensity profile obtained from the diffraction rings is superimposed on the image. The most intense reflections originate from crystalline Cu. Additional reflections originate from Ru and CuO. Note that some of the Ru reflections are overlapped with those of CuO. The brightness and contrast of a part of the image was adjusted for better visibility of some reflections.

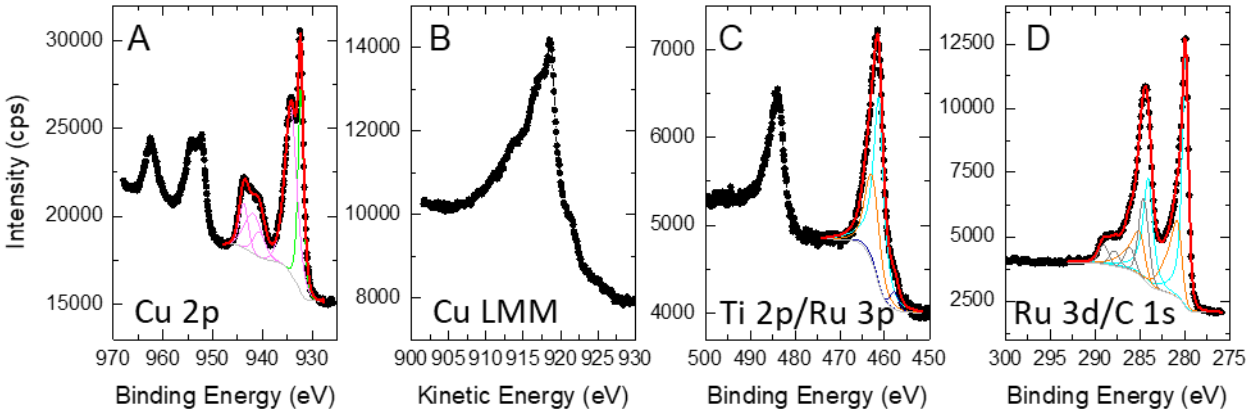

Figure S4. XPS data of as prepared Cu-Ru/Ti electrode collected over the energy ranges typical for (A) Cu 2p, (B) Cu LMM, (C) Ru 3p (overlapping with Ti 2p) and (D) Ru 3d (overlapping with C 1s) signals, collected on the pristine sample without further treatments.

Fitting of the data in Figure 4A evidenced the presence of two different oxidation states for copper. The Cu 2p satellites at approx. 940 – 945 eV, together with the broad and intense peak at 934.3 eV (magenta profiles), are a clear indication of Cu(II) compounds, most likely in the form of CuO or $Cu(OH)_2$;[1] the narrow component at 932.3 eV (green line) could be instead assigned to either Cu(I) and Cu(0) species. The analysis of the Cu LMM Auger spectrum in Figure 4B, characterized by the presence of the narrow peak at 918.6 eV, allowed us to assign that component to Cu(0).[1] The analysis of the Ru signals (both Ru 3p and Ru 3d spectra) was performed following literature reports on catalytically and technologically relevant Ru compounds.[2] To obtain the best fit of our data, we had to assume the presence of two different oxidation states for Ru. In particular, the fitting was done using lineshapes as optimized in the reference for metallic Ru (cyan peaks in panels C and D) and hydrated RuO_2 (orange peaks in the same panels).[2] Metallic Ru was the predominant species, as it accounted for more than 65% of the Ru content at the sample's surface. In panel C, the analysis revealed also the presence of low intensity peaks related to Ti, centered at 457.7 eV and 463.4 eV (±0.3 eV) and indicating the presence of TiO_x species.[3] As previously discussed, TiO_x formed by etching of the Ti substrate under alkaline conditions.[4] In panel D, four carbon peaks, centered at 284.6 eV, 286.5 eV, 287.9 eV and 289.1 eV and accounting respectively for C-C, C-O, C=O and O-C=O bonds, were added to obtain the best fit to the experimental data.[5] These species are likely due to environmental contaminations.

X-ray absorption measurements

XAS is an average element-specific technique which provides electronic (XANES) and structural information (EXAFS) of a variety of systems regardless of their physical state (gas, liquid, solid), crystallinity degree or dilution regime. The technique is based on the photoelectric absorption process and the absorption coefficient of the sample, probed as a function of photon energy, is sensitive to the environment of the absorbing atom. The phenomena occurring near the absorption edge (energy in which an electron of an atomic shell can be ejected, for example 22117 eV for K-edge electron of Ru) are comprised in the X-ray Absorption Near Edge Structure (XANES) spectral region. This technique probes the unoccupied bound states, providing information about the electronic properties of the absorber, often a fingerprint to determine oxidation states and site symmetry of the element of interest. At higher photon energies (>50 keV), the ejected photoelectron may be back-scattered by the neighbouring atoms, creating the oscillations in the absorption coefficient, the EXAFS oscillations, which contain the local structural information.[6] Here, we explored XAS in order to improve our understanding about the electronic and structural properties of Ru species in the catalysts.

Table S1. First-shell structural parameters (Coordination Numbers, Interatomic Distances, and Debye-Waller factors) for the samples at Ru K- edge, and the metallic bulk Ru reference.

Sample	Absorber-Scatterer	CN	R (Å)	σ^2 (Å^2)	R-factor
Ru foil	Ru-Ru	12.0[(a)]	2.676 (0.003)	0.004 (0.001)	0.008
Ru/Ti	Ru-O	2.4 (0.8)	1.919 (0.030)	0.009 (0.003)	0.015
	Ru-Ru	9.2 (1.1)	2.671 (0.005)	0.005 (0.001)	
Cu-Ru/Ti	Ru-O	3.9 (1.2)	1.987 (0.015)	0.007 (0.005)	0.030
	Ru-Ru	6.1 (1.1)	2.671 (0.009)	0.007 (0.001)	

(a) Fixed.

Figure 3E compares the Ru-K edge X-ray absorption near edge structure (XANES) spectra of the Ru/Ti and Cu-Ru/Ti samples with the Ru^0 and RuO_2 reference compounds. It can be observed that both samples show features similar to those of Ru^0, including the energy position at which the sharp increase in absorption (edge) occurs. The comparison of the energy position with references is commonly employed to identify the average oxidation state of the absorber atom in the sample.[7] In the case of Ru/Ti and Cu-Ru/Ti, the edge energy showed no shift towards higher energies (in the direction of the one observed for RuO_2), matching that of the Ru^0 reference and, thus, indicating that the average oxidation state of Ru in Ru/Ti and Cu-Ru/Ti is 0.

The features observed in XANES spectra are due to the excitation of the core electrons to any empty state, starting from the lowest empty state. The XANES at Ru-K edge essentially probes the local empty density of states of p symmetry in the Ru absorber, providing insights into electronic changes that might occur in Ru atoms (due to nanosizing or interaction with heteroatoms).[7, 8] Therefore, it was possible to obtain information about the electronic nature of Ru by comparing the XANES spectra of pure Ru^0, Ru/Ti and Ru-Cu/Ti samples. As shown in Figure 3E, where a closer view of the 22100-22170 eV range is reported, the

XANES spectra illustrate three main features, labelled as “a”, “b” and “c”. The feature “a” arises from transitions occurring in the mixed 5p-4d levels of Ru, [7, 8] and its decrease has been associated to the lack of a long-range order, or to a slight oxidation of Ru atoms in Ru-based bimetallic structures. In both cases, Ru^0 was kept as the average valence state. [8, 9] The trends in the “a” peak in our Ru/Ti and Cu-Ru/Ti samples (if compared to the Ru^0 reference, see Figure 3E), thus suggested a lack of long-range order in the Ru domains and/or a minor oxidation of Ru species. Moreover, in previous works on bimetallic Ru-Pt or Ru-Co compounds/materials a broadening of the Ru signal between “b” and “c” features (accompanied by the decrease of “a” and “c” features and the increase of “b” features) have been clearly observed. [9, 10] The authors correlated the XANES features to the nanometric nature of Ru domains and the increase in empty 5p states compared to the monometallic counterparts, which could also be attributed to our samples. [9, 10]
Interestingly, an analogous trend in XANES as observed when comparing Ru/Ti to Cu-Ru/Ti, was previously demonstrated for reasonably homogeneous bimetallic RuPt nanostructures, evidencing intermetallic Ru-Pt bonds. [11-13] Therefore, Ru-K edge XANES qualitatively suggest that there is an interaction between Ru and Cu atoms, especially when comparing Ru/Ti and Cu-Ru/Ti samples.
Depending on the degree of their interaction, which may vary according to the specific architecture adopted (homogeneous alloys, core-shell structures, segregated monometallic clusters), a charge transfer should occur between Cu and Ru atoms, with Ru typically accepting excess electrons from Cu. [14, 15] However, probing the Ru-K edge can essentially provide information regarding the Ru 5p empty states, which is not sufficient to identify the overall charge transfer occurring between the Ru and Cu atoms. [7]
In order to obtain information on the local structure of the Ru domains at the atomic level we acquired and compared the extended X-ray absorption fine structure (EXAFS) structural data (Figure S5A and Table S1) of Ru/Ti, Cu-Ru/Ti samples and Ru^0 and RuO_2 references. In the 1-2 Å region we could identify the Ru-O scattering from RuO_2, while for Ru^0 the first Ru-Ru shell was detected between 2 Å and 3 Å. Both Ru/Ti and Cu-Ru/Ti samples showed minor Ru-O contributions with a predominance of Ru-Ru interactions. No specific/particular other features, which could be ascribed to Ru-Cu contributions, were observed in EXAFS structural data. Copper and ruthenium are known to be immiscible, [14, 16] therefore the local environment of Ru absorber (fraction of Ru or Cu neighbors), as probed by the average EXAFS signal, can vary depending on the segregation degree of Ru and Cu elements. [17] The structural EXAFS analysis is heavily influenced by polydispersity and inhomogeneity of bimetallic samples, [18] which seems to be the case of Ru domains in the Cu-Ru/Ti sample. Accordingly, the heterogeneous nature of the Ru domains would also explain the lack of drastic differences in the XANES features between Ru/Ti and Cu-Ru/Ti. The XAS analysis at the Cu-K edge did not show any difference between Cu/Ti and Cu-Ru/Ti samples (see Figure S5 B and C), due to the low Ru/Cu ratio (0.02) and the consequent small amount of Cu atoms in direct contact with Ru ones. Hence, the XAS results show the short-range order of Ru domains in both Ru/Ti and Cu-Ru/Ti samples, as well as suggests changes in electronic properties of Ru in the presence of Cu.

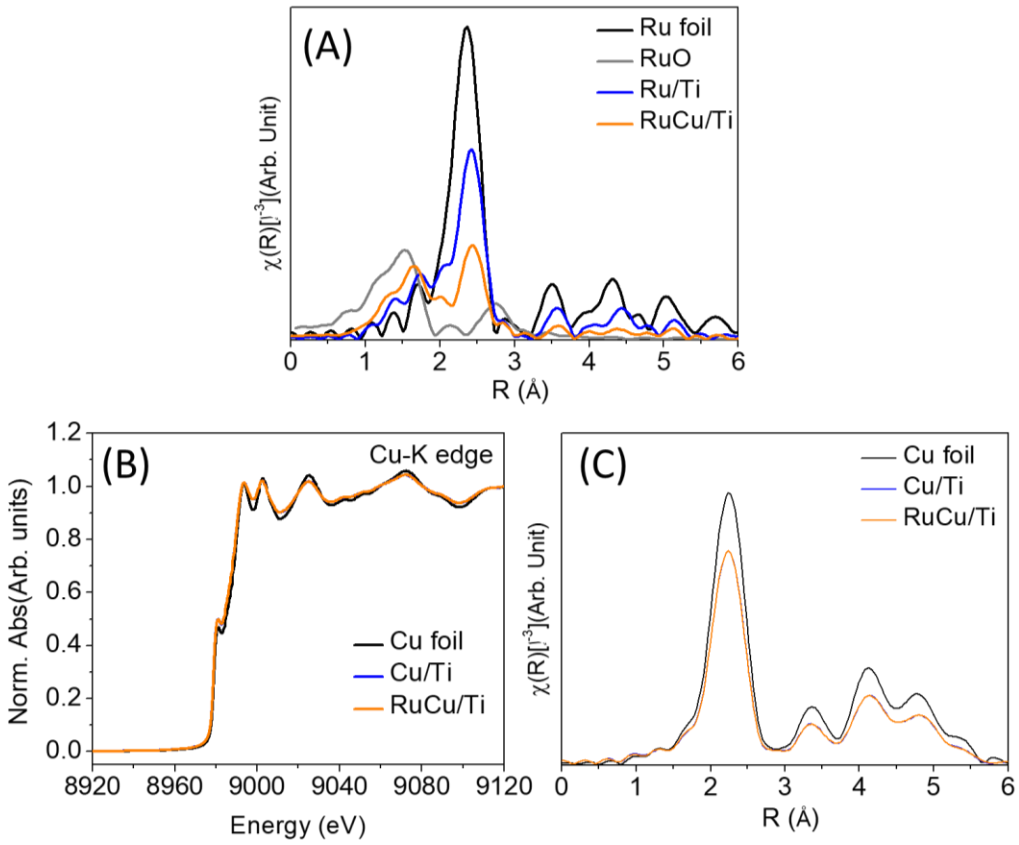

Figure S5. A) Magnitude of the Fourier transformed k^2-weighted Ru K-edge EXAFS of various samples. B) XANES spectra at Cu-K edge C) Fourier transform of k3-weighted Cu EXAFS spectra.

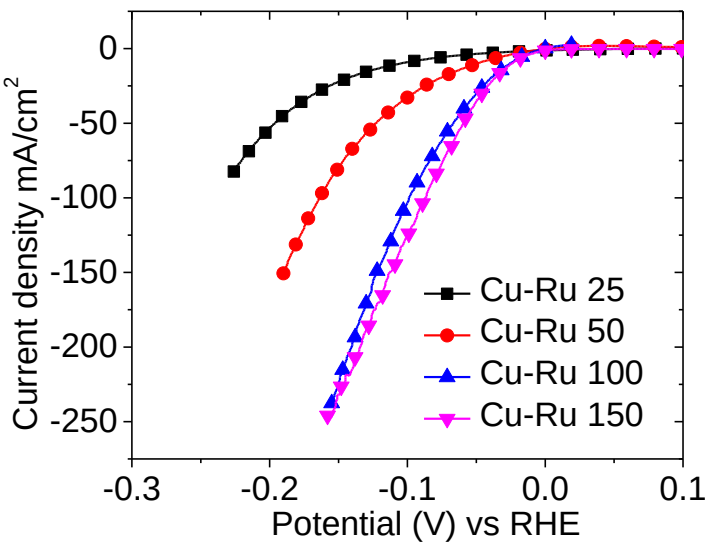

Figure S6. Linear sweep voltammograms of Cu-Ru/Ti catalysts with various Ru loadings. The Ru loadings were controlled by amount of K_2RuCl_6 solution added in the electrolyte for the electrodeposition.

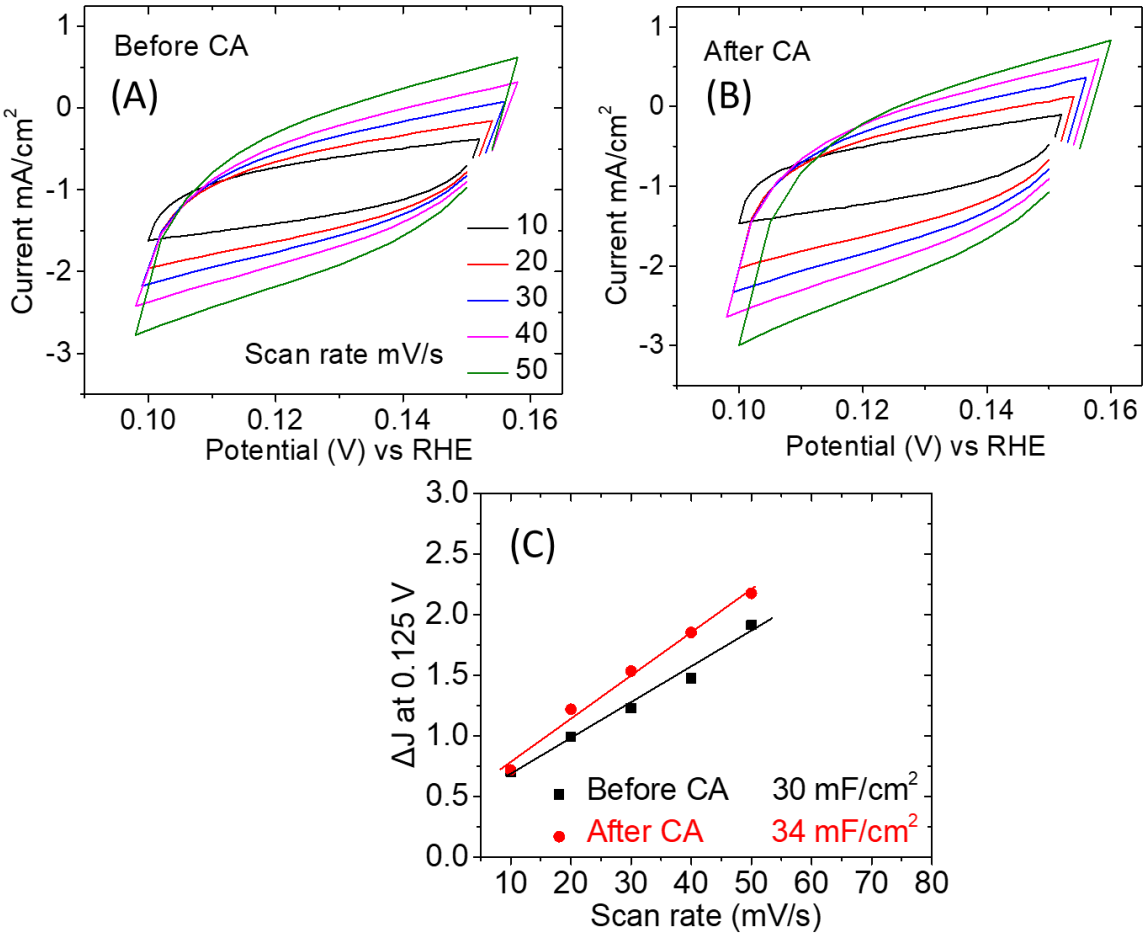

Figure S7. Measurement of the electrochemically active surface area of Cu-Ru/Ti electrode before and after CA test for 100 h. A), B) CV curves at different scan rates measured before and after CA and C) J_{anodic} + $J_{cathodic}$ at 0.125 V plotted vs scan rate. The slope of the resulting line is equal to double layer capacitance of the electrode.

Calculation of mass and price activity

Mass activity

The mass activity of Cu-Ru/Ti electrode was calculated at an applied potential of -0.1V by only considering the mass of Ru, as Cu/Ti electrode did not exhibit any HER current at this potential. This was done by subtracting the value of background current produced by Cu/Ti electrode from the current produced by Cu-Ru/Ti electrode.

$$j_{mass}^{Cu-Ru/Ti} = \frac{j_{area}^{Cu-Ru/Ti} - j_{area}^{Cu/Ti}(A\ cm^{-2})}{mass_{Ru}} = \frac{0.104 - 0.002\ (A\ cm^{-2})}{0.063\ (mg\ cm^{-2})}$$

$$= 1.619\ \ (A\ mg^{-1})$$

$$j_{mass}^{Pt/C} = \frac{j_{area}^{Pt/C}(Acm^{-2})}{mass_{Pt}} = \frac{0.033\ (A\ cm^{-2})}{0.05\ (mg\ cm^{-2})}$$

$$= 0.66\ \ (A\ mg^{-1})$$

Price activity

The price activity of various catalysts was calculated by using the prices of noble metals as reported previously:[19]

$$j_{price}^{Cu-Ru/Ti} = \frac{mass\ activity_{Cu-Ru/Ti}}{price_{Ru}} = \frac{1.619 * 10^3\ \ (A\ g^{-1})}{6.88\ \ (dollar\ g^{-1})} = 235.3\ \ A\ dollar^{-1}$$

$$j_{price}^{Pt/C} = \frac{mass\ activity_{Pt/C}}{price_{Pt}} = \frac{0.66 * 10^3\ \ (A\ g^{-1})}{34.36\ \ (dollar\ g^{-1})} = 19.2\ \ A\ dollar^{-1}$$

Table S2. Comparison of HER activity in terms of overpotential to achieve 10 mA/cm^2 of catalytic current and Tafel slopes of various highly active catalysts reported in the literature.

Catalyst	Electrolyte	Catalyst loading (mg/cm^2)	Overpotential (mV) at 10 mA/cm^2	Tafel slope (mV/dec)	Reference
Cu-Ru/Ti	1 M NaOH	1.953	23	34	This work
Sr_2RuO_4	1 M KOH	0.232	61	51	[19]
$Ru@C_2N$	1 M KOH	0.285	17	38	[20]
RuP_2@NPC	1 M KOH	1	52	69	[21]
NiRu@NC	1 M KOH	0.273	32	64	[22]
$Ni_{1.5}Co_{1.4}P$@Ru	1 M KOH	0.28	52	50	[23]
$Cu_{2-x}S$@Ru NPs	1 M KOH	0.23	48	82	[24]
Ru/MoS_2	1 M KOH	~1	13	60	[25]
1D $RuO_2@CN_x$	1 M KOH	0.212	95	70	[26]
S-CoO NRs	1 M KOH	0.486	73	82	[27]
Ni-BDT-A	1 M KOH	1	80	70	[28]
Fe-CoP	1 M KOH	1.03	78	75	[29]
CoP-MNA	1 M KOH	6.2	54	51	[30]
α-Ni_3S_2@NPC	1 M KOH	N.A.	61	68	[31]
$Mo_2C@C$	1 M KOH	0.9	50	71	[32]

Table S3. Comparison of long-term operational stability of various highly active HER catalyst based on PGMs.

Catalyst	Electrolyte	Stability	Reference
Pt-N-doped graphene	0.5 M H_2SO_4	2.7 h at -0.04 V; 70% retention*	[33]
Pt-$(NiOH)_2$	0.1 M KOH+ 0.1M LiOH	2.25 h at -0.11 V; 81% retention*	[34]
Pt NWs-$(NiOH)_2$	1M KOH	1.1 h at -0.077V; 95.7% retention	[35]
Pt3Ni3 NWs	1 M KOH	3 h at -0.077 V; 90.1% retention	[36]
Hcp-PtNi	0.1 M KOH	1 h at -0.065 V; 45 % retention	[37]
Pt-$Ni(OH)_2$	0.1 M LiOH	3 h at -0.1 V; 49% retention*	[38]
Pt-Polyoxometalate	0.5 H_2SO_4	12 h at –0.1V; 10% retention	[39]
Pt-Mesoporous C	1M KOH	5 h at –0.15V; 95% retention	[40]
Fcc Ru	0.1M KOH	50 h at -0.05 ; 90% retention	[41]
Ru_2P@NPC	1M KOH	10 h at -0.053; 70% retention	[21]
Pt/C	1 M NaOH	24 h at -0.2V; 19% retention	This Work
Cu-Ru/Ti	1 M NaOH	100 h at -0.2V; 100% retention	This Work

*Values estimated from graphs

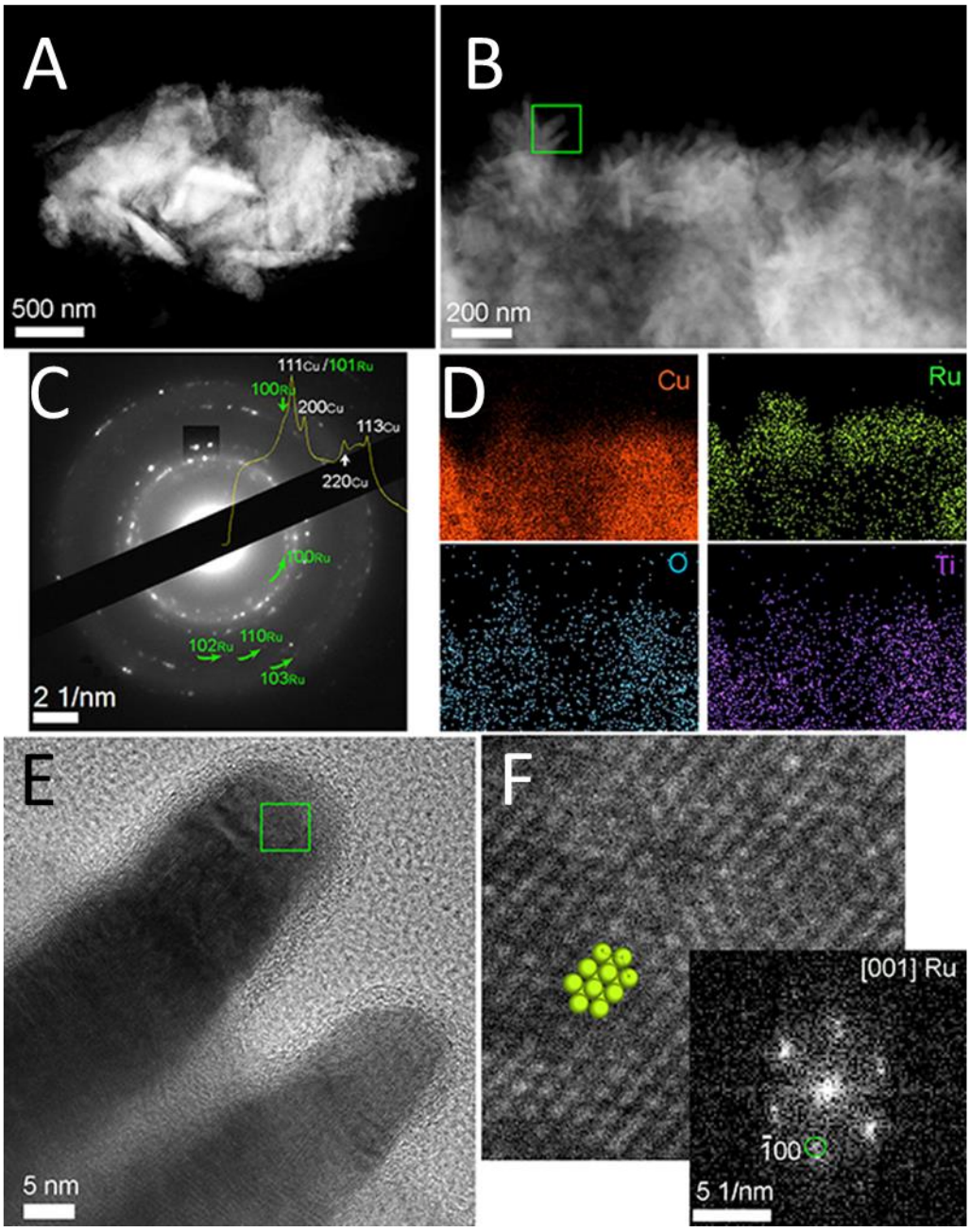

Figure S8. TEM characterization of the catalyst after 100 hrs of continuous H_2 evolution. A) STEM image of an aggregate of polycrystalline Cu NPls B) enlarged view of the top part of the aggregate showing elongated NCs extending from the surface. C) TEM electron diffraction pattern from the catalysts indexed according to Cu (strongest reflections) and Ru crystal structures. D) EDX elemental maps Cu, Ru, O and Ti corresponding to the STEM image in B) indicate that the elongated NCs on the surface of the Cu flakes are Ru-rich. E) HRTEM image from two Ru NCs (outlined by a green rectangle in B. Corresponding FFT from one of the NCs is shown in F) (lower panel) and indexed according to hexagonal structure of elemental Ru. An enlarged section from one of the Ru NCs is shown in the upper panel in F); overlaid on top of this image is the model of Ru atom arrangement in the same orientation as observed experimentally.

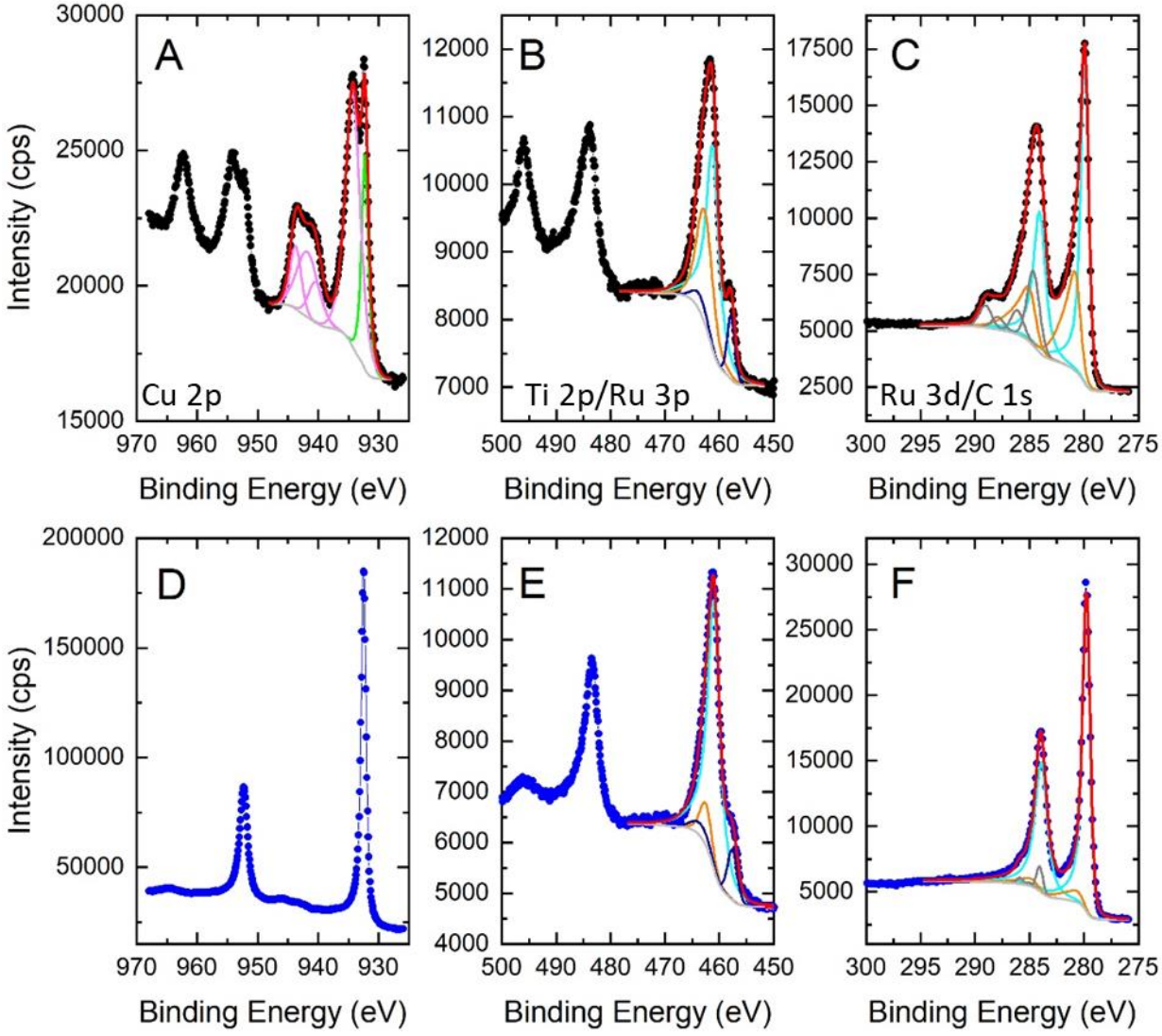

Figure S9. XPS analysis of the Cu-Ru/Ti electrode after 100 h stability test at -0.2V (A-C) pristine sample and (D-F) after Ar^+ sputtering to remove the surface layer.

Supporting references

1. M. C. Biesinger, *Surf. Interface Anal.*, 2017, **49**, 1325-1334.
2. D. J. Morgan, *Surf. Interface Anal.*, 2015, **47**, 1072-1079.
3. M. C. Biesinger, L. W. M. Lau, A. R. Gerson and R. S. C. Smart, *Appl. Surf. Sci.*, 2010, **257**, 887-898.
4. D. V. Shinde, Z. Dang, U. Petralanda, M. Palei, M. Wang, M. Prato, A. Cavalli, L. De Trizio and L. Manna, *ACS Appl. Mater. Interfaces*, 2018, **10**, 29583-29592.
5. G. Beamson, *John Wiley and Sons, Toronto*, 1992, **Appendices 1-3**.
6. M. Newville, *Rev. Mineral. Geochem.*, 2014, **78**, 33-74.
7. F. M. F. de Groot, *J. Phys.: Conf. Ser.*, 2009, **190**, 012004.
8. Z. Wu, N. L. Saini, S. Agrestini, D. D. Castro, A. Bianconi, A. Marcelli, M. Battisti, D. Gozzi and G. Balducci, *J. Phys.: Condens. Matter*, 2000, **12**, 6971-6978.
9. L. Zhang, R. Si, H. Liu, N. Chen, Q. Wang, K. Adair, Z. Wang, J. Chen, Z. Song, J. Li, M. N. Banis, R. Li, T.-K. Sham, M. Gu, L.-M. Liu, G. A. Botton and X. Sun, *Nat. Commun.*, 2019, **10**, 4936.
10. D. Bazin, I. Kovács, J. Lynch and L. Guczi, *Appl. Catal. A-Gen.*, 2003, **242**, 179-186.
11. S. Alayoglu, P. Zavalij, B. Eichhorn, Q. Wang, A. I. Frenkel and P. Chupas, *ACS Nano*, 2009, **3**, 3127-3137.
12. H. Wang, S. Chen, C. Wang, K. Zhang, D. Liu, Y. A. Haleem, X. Zheng, B. Ge and L. Song, *J. Phys. Chem. C*, 2016, **120**, 6569-6576.
13. L. M. Kustov, E. D. Finashina, V. I. Avaev and B. G. Ershov, *Fuel Process. Technol.*, 2018, **173**, 270-275.
14. R. Fukuda, N. Takagi, S. Sakaki and M. Ehara, *J. Phys. Chem. C*, 2017, **121**, 300-307.
15. Y. Li, W. Zhou, X. Zhao, W. Cheng, H. Su, H. Zhang, M. Liu and Q. Liu, *ACS Appl. Energy Mater.*, 2019, **2**, 7483-7489.
16. J. Liu, L. L. Zhang, J. Zhang, T. Liu and X. S. Zhao, *Nanoscale*, 2013, **5**, 11044-11050.
17. A. I. Frenkel, *Chem. Soc. Rev.*, 2012, **41**, 8163-8178.
18. J. Moonen, J. Slot, L. Lefferts, D. Bazin and H. Dexpert, *Physica B: Condensed Matter*, 1995, **208-209**, 689-690.
19. Y. Zhu, H. A. Tahini, Z. Hu, J. Dai, Y. Chen, H. Sun, W. Zhou, M. Liu, S. C. Smith, H. Wang and Z. Shao, *Nat. Commun.*, 2019, **10**, 149.
20. J. Mahmood, F. Li, S.-M. Jung, M. S. Okyay, I. Ahmad, S.-J. Kim, N. Park, H. Y. Jeong and J.-B. Baek, *Nat. Nanotechnol.*, 2017, **12**, 441-446.
21. Z. Pu, I. S. Amiinu, Z. Kou, W. Li and S. Mu, *Angew. Chem. Int. Ed.*, 2017, **56**, 11559-11564.
22. Y. Xu, S. Yin, C. Li, K. Deng, H. Xue, X. Li, H. Wang and L. Wang, *Journal of Materials Chemistry A*, 2018, **6**, 1376-1381.
23. S. Liu, Q. Liu, Y. Lv, B. Chen, Q. Zhou, L. Wang, Q. Zheng, C. Che and C. Chen, *ChCom*, 2017, **53**, 13153-13156.
24. D. Yoon, J. Lee, B. Seo, B. Kim, H. Baik, S. H. Joo and K. Lee, *Small*, 2017, **13**, 1700052.
25. J. Liu, Y. Zheng, D. Zhu, A. Vasileff, T. Ling and S.-Z. Qiao, *Nanoscale*, 2017, **9**, 16616-16621.
26. T. Bhowmik, M. K. Kundu and S. Barman, *ACS Appl. Mater. Interfaces*, 2016, **8**, 28678-28688.
27. T. Ling, D.-Y. Yan, H. Wang, Y. Jiao, Z. Hu, Y. Zheng, L. Zheng, J. Mao, H. Liu, X.-W. Du, M. Jaroniec and S.-Z. Qiao, *Nat. Commun.*, 2017, **8**, 1509.
28. C. Hu, Q. Ma, S.-F. Hung, Z.-N. Chen, D. Ou, B. Ren, H. M. Chen, G. Fu and N. Zheng, *Chem*, 2017, **3**, 122-133.
29. C. Tang, R. Zhang, W. Lu, L. He, X. Jiang, A. M. Asiri and X. Sun, *Adv. Mater.*, 2017, **29**, 1602441.
30. Y.-P. Zhu, Y.-P. Liu, T.-Z. Ren and Z.-Y. Yuan, *Adv. Funct. Mater.*, 2015, **25**, 7337-7347.
31. C. Yang, M. Y. Gao, Q. B. Zhang, J. R. Zeng, X. T. Li and A. P. Abbott, *Nano Energy*, 2017, **36**, 85-94.

32. Y.-Y. Chen, Y. Zhang, W.-J. Jiang, X. Zhang, Z. Dai, L.-J. Wan and J.-S. Hu, *ACS Nano*, 2016, **10**, 8851-8860.
33. N. Cheng, S. Stambula, D. Wang, M. N. Banis, J. Liu, A. Riese, B. Xiao, R. Li, T.-K. Sham, L.-M. Liu, G. A. Botton and X. Sun, *Nat. Commun.*, 2016, **7**, 13638.
34. R. Subbaraman, D. Tripkovic, D. Strmcnik, K.-C. Chang, M. Uchimura, A. P. Paulikas, V. Stamenkovic and N. M. Markovic, *Science*, 2011, **334**, 1256-1260.
35. H. Yin, S. Zhao, K. Zhao, A. Muqsit, H. Tang, L. Chang, H. Zhao, Y. Gao and Z. Tang, *Nat. Commun.*, 2015, **6**, 6430.
36. P. Wang, K. Jiang, G. Wang, J. Yao and X. Huang, *Angew. Chem. Int. Ed.*, 2016, **55**, 12859-12863.
37. Z. Cao, Q. Chen, J. Zhang, H. Li, Y. Jiang, S. Shen, G. Fu, B.-a. Lu, Z. Xie and L. Zheng, *Nat. Commun.*, 2017, **8**, 15131.
38. L. Wang, C. Lin, D. Huang, J. Chen, L. Jiang, M. Wang, L. Chi, L. Shi and J. Jin, *ACS Catal.*, 2015, **5**, 3801-3806.
39. C. Zhang, Y. Hong, R. Dai, X. Lin, L.-S. Long, C. Wang and W. Lin, *ACS Appl. Mater. Interfaces*, 2015, **7**, 11648-11653.
40. H. Zhang, P. An, W. Zhou, B. Y. Guan, P. Zhang, J. Dong and X. W. Lou, *Sci. Adv.*, 2018, **4**, eaao6657.
41. Y. Zheng, Y. Jiao, Y. Zhu, L. H. Li, Y. Han, Y. Chen, M. Jaroniec and S.-Z. Qiao, *J. Am. Chem. Soc.*, 2016, **138**, 16174-16181.